Welding in the World (2024) 68:939–951
https://doi.org/10.1007/s40194-024-01695-8

RESEARCH PAPER

# Effect of solution heat treatment on the microstructure and mechanical properties of laser melting deposited GH 5188 superalloy

**Yan Wang[1] · Wei Liu[1] · Shuai Huang[1] · Chao Gao[1] · Neng Li[1] · Huaping Xiong[1]**

Received: 15 August 2023 / Accepted: 21 January 2024 / Published online: 12 February 2024


**Abstract**
GH 5188 is a solution strengthening cobalt-based superalloy, which is widely used for manufacturing hot components with service temperatures of 1000 ~ 1100 °C. GH 5188 superalloy was fabricated by laser melting deposition (LMD) followed by solution treatment. The effect of heat treatment temperature ranging from 1140 to 1260 ℃ on microstructure and tensile properties of as-LMD specimens was investigated. Optical microscope (OM) and scanning electron microscope (SEM) were used for microstructural observation, and transmission electron microscope (TEM) was employed for phase determination. The results showed that heat treatment did not affect phases within the as-LMD GH 5188 specimens, which were composed of γ, $M_{23}C_6$, $M_6C$, and $La_2O_2C_2$, whereas heat treatment temperature had an evident effect on the size and content of carbides. In general, heat treatment improved both the ultimate tensile strength (UTS) and the elongation (EL) of as-LMD specimens. With the increase of heat treatment temperature varying from 1140 to 1260 ℃, the UTS enhanced firstly to 1051.9 MPa and then decreased to 934.8 MPa. As the reason, Carbide dispersion distribution contributed to the increase of UTS below the heat treatment at 1180 ℃, and the decrease of volume fraction and size for carbide led to the decrease of UTS above the heat treatment at 1180 ℃. The EL increased slightly at first and then rose rapidly. On the contrary, YS monotonously decreased from 587.1 to 503.6 MPa. The dimples became deeper as the heat treatment temperature increased, indicating better toughness.

**Keywords** Laser melting deposition · GH 5188 · Microstructure · Heat treatment · Tensile properties

## 1 Introduction

GH 5188 is a solution strengthening cobalt-based superalloy with the addition of 13–16% tungsten, 20–24% chromium, and trace lanthanum, which is known for its ability of excellent high-temperature thermostability and oxidation resistance, satisfactory formability, and weldability [1–3]. Based on the above advantages, it is suitable for fabricating hot components with the service temperature of about 1000 ℃ [4–6]. Hence, this cobalt-based superalloy was widely used in gas turbines, nuclear power, aero-engine, and aerospace such as combustion chambers, heat exchangers, flame tubes, and exhaust nozzle [7–9].

At present, conventional methods for GH 5188 superalloy, such as casting and forging, were used in manufacturing process of majority components. However, these conventional methods, usually, not only waste materials but also increase the fabrication cost and time [10–12].

Additive manufacturing (AM) is defined as "the process of joining materials" usually layer by layer to make

Highlights.

(1) GH5188 samples were fabricated by LMD, and effects of heat treatment on microstructure and properties were studied.

(2) Heat treatment had an evident effect on the size and content of carbides but nearly no effect on the phase of the as-LMD samples.

(3) HT improved both strength and elongation of specimens, and all HT samples exhibited a ductile fracture feature.

✉ Neng Li
lineng621@163.com

✉ Huaping Xiong
xionghp69@163.com; xionghuaping69@sina.cn

[1] Division of Welding and Plastic Forming, 3D Printing Research & Engineering Technology Center, Beijing Institute of Aeronautical Materials, Beijing 100095, China

the near-formed dense metal parts with complex shape from 3D model data [13–15]. Compared with the conventional cutting process, it shows a lot of advantages including high manufacturing flexibility and short production cycle as well as low costs [16,17]. Laser metal deposition (LMD) is a typical additive manufacturing technique that is widely applied to various high-temperature alloys, such as Inconel 625 [18], Inconel 718[19], Hastelloy X [20], and Inconel 100 [21]. LMD is characterized by rapid heating and cooling induced by the large temperature gradient, which can generate the supersaturated solid solution [22,23]. Cr-rich and W-rich carbides will precipitate in the unstable supersaturated sod solution at the elevated temperature. As is well-known, the size, content, distribution, and morphology of Cr-rich and W-rich carbides play a significant role on the mechanical properties [24].

In general, to obtain the desired mechanical properties and ideal microstructure, heat treatment is necessary which can not only adjust the microstructure features [25] but also decrease the level of residual stresses and eliminate element segregation [26–28].

Several studies have been reported on additive manufacturing of GH 5188; for example, Wei et al. [29,30] investigated the microstructure and mechanical properties of SLM-fabricated GH 5188 Co superalloy. The results showed that fine eutectic carbides were formed in as-SLM specimens and as-SLM specimens exhibited excellent strength and ductility compared with forging and casting samples. Additionally, it was also found that horizonal samples had a higher ductility compared with vertical samples. Xu et al. and Liu et al. [31,32] discussed the effect of processing parameters on the density of SLM GH 5188, and the results showed that with the energy density increases, density of specimens firstly increased and then decreased, and the hardness and elongation increased significantly. Also, researchers mainly focused on the microstructure and mechanical properties of GH 5188 manufactured via ultrasonic-assisted laser powder bed fusion[33]. The results showed that ultrasonic vibration could refine the grain and inhibit the preferred orientation of texture to improve the mechanical properties. Eissel et al. [[34]] reported that the Co–Cr alloy with different contents of Ti and Zr up to 1 wt% exhibited significant effects on the welded solidification morphology, as well as the subsequent machinability. However, no study focused on the effect of the heat treatment on the microstructure and mechanical properties of GH 5188 fabricated by AM. Meanwhile, as a solid solution strengthening superalloy, the optimization of temperature should have a significant impact on microstructure and mechanical properties of GH5188.

In this study, different heat treatment temperatures were conducted on the as-LMD GH 5188 specimens. Meanwhile, the relationship between heat treatment temperature, the microstructure, and mechanical properties of as-LMD GH 5188 specimens was discussed.

## 2 Experimental procedures

### 2.1 Powder materials

The gas atomized GH 5188 powder supplied by Avimetal Power Metallurgy Technology Co. Ltd. was used as the feedstock material in this study. The chemical composition in weight percentage (wt. %) is Co (balance), Cr (22.78), Ni (22.64), W (14.56), Fe (1.21), Si (0.42), Mn (1.00), C (0.10), and La (0.02). The particle size distribution with D10 of 57.0 μm, D 50 of 78.6 μm, and D 90 of 108.5 μm was obtained by Malvern MS 2000 HYDRO 2000MU software (Fig. 1a). The powder morphology was shown in Fig. 1b and c.

### 2.2 LMD process

GH 5188 specimens were fabricated by a LMD equipment, which consisted of a powder feeder system, working table, and YLR-6000 fiber laser. Laser deposition parameters used in the experiment were listed in Table 1. A 90° rotation of scanning strategy between adjacent deposited layers

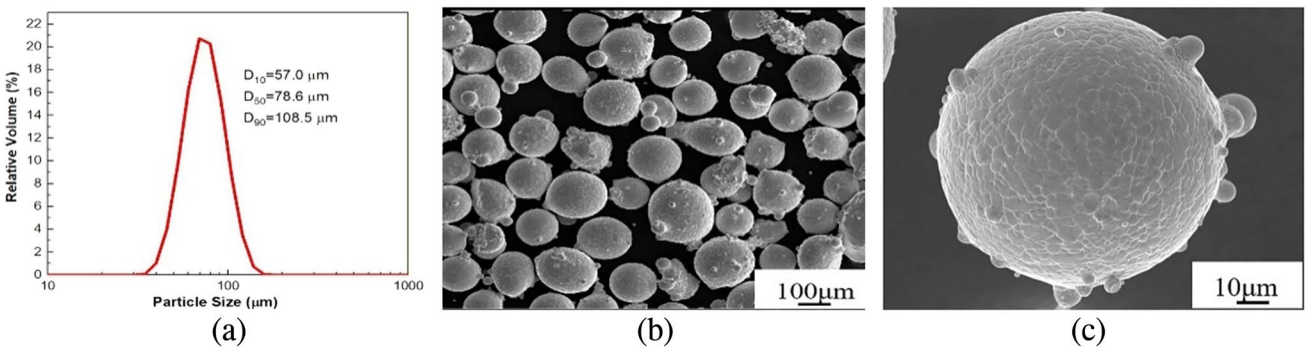


**Fig. 1** Particle size distribution (**a**) and SEM images at low (**b**) and high magnification (**c**) of GH 5188 powders

**Table 1** Laser deposition parameters used in the experiment

| Laser power | Laser scanning speed | Powder feed rate | Spot diameter | Argon gas flow rate | Overlap rate |
|---|---|---|---|---|---|
| 500 W | 600 mm/min | 3 g/min | 0.3 mm | 20 L/min | 50% |

**Table 2** Heat treatment procedure for the as-LMD GH 5188 specimens

| Condition | Heat treatment process | Cooling method |
|---|---|---|
| LMD GH 5188 | – | – |
| Heat-treated (HT) specimens | LMD + 1140 °C/30 min | Wind cooling |
| | LMD + 1180 °C/30 min | |
| | LMD + 1220 °C/30 min | |
| | LMD + 1260 °C/30 min | |

was applied to eliminate anisotropy on the *X*–*Y* plane. A wrought GH 5188 sheet was used as the substrate, with a thickness of 12 mm. As-LMD specimens with the dimension of 45 mm × 15 mm × 8 mm were fabricated by LMD equipment.

### 2.3 Heat treatment and microstructure characterization

Based on the knowledge of wrought counterpart, as-LMD specimens were subjected to the heat treated at different temperatures at 1140 ℃, 1180 ℃, 1220 ℃, and 1260 ℃ for 30 min followed by wind cooling to room temperature. The heat treatment procedure was given in Table 2. A controlled atmosphere furnace without quenching ability for the treatment and a fan with a speed of 8 m/s was adopted for the cooling process.

Metallographic specimens were cut horizontally to the building direction from the as-LMD specimens and HT specimens and subsequently prepared according to standard procedures. Finally, specimens were etched by a solution of 5 mL $H_2O_2$ + 100 mL HCl for 10 s. The microstructure of as-LMD specimens and HT specimens was analyzed with an optical microscope (OM) and scanning electron microscope (SEM) equipped with energy-dispersive X-ray spectrometer (EDS). The grain size was determined by linear intercept method, and the reported values were the result of 20 intercept experiments. The size and volume fraction of carbides were recorded by Image-Pro Plus software, and reported values were calculated from 10 SEM images at 2000 times. The detailed microstructure was examined by the Tecnai G2F20 transmission electron microscope (TEM). These specimens were prepared firstly by thinning down mechanically to thin foils with a thickness of 70 μm and then punched 3-mm-diameter disks from the foils. Finally, these disks were thinned by ion milling.

### 2.4 Mechanical property test

The tensile test was conducted at room temperature using an Instron 5887 universal tensile testing machine with ISO 6892–1 specimens. The size of tensile tested specimen was shown in Fig. 2. The reported value was the average values of ultimate tensile stress (UTS), yield stress (YS), and elongation (EL) from three measured specimens for each case.

## 3 Results and discussion

### 3.1 Microstructure of LMD GH 5188

OM image of as-LMD GH 5188 specimens was shown in Fig. 3a that columnar structure with the orientation of ~ 45–50° to the substrate was observed in all layers.

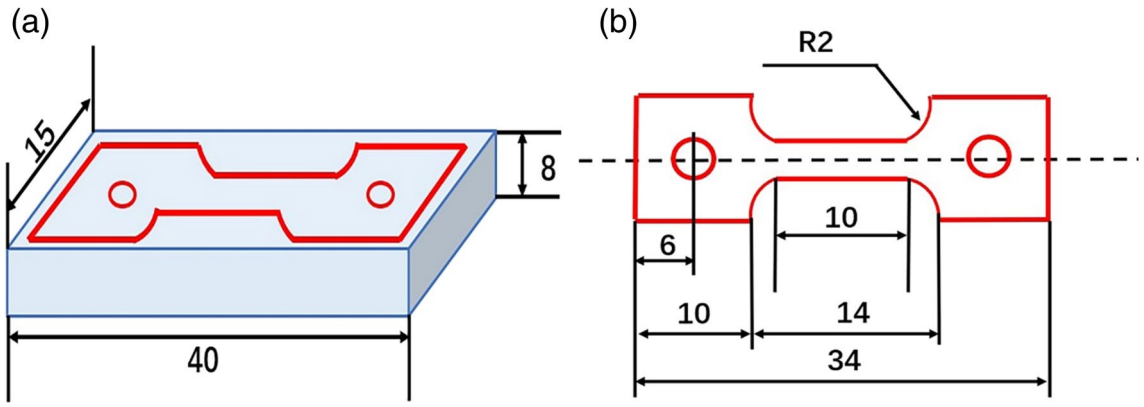


**Fig. 2** Dimensions of as-LMD GH 5188 samples (**a**) and sketch of tensile samples (**b**)

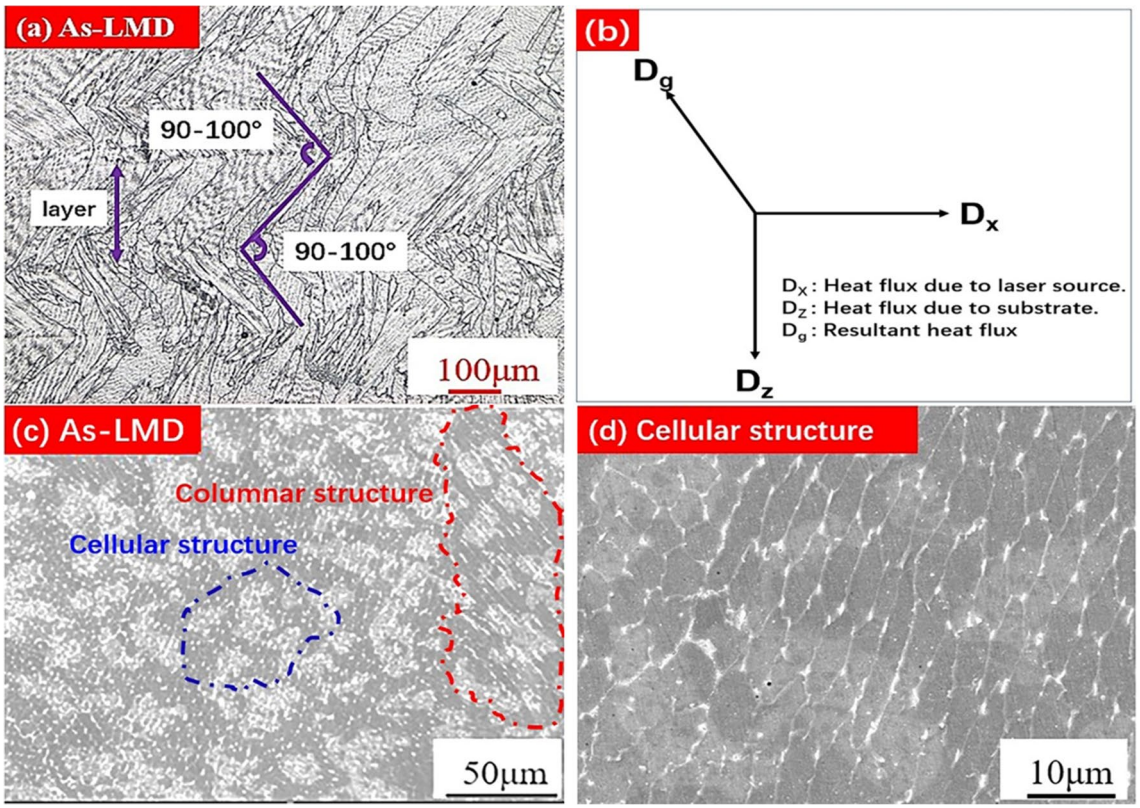


**Fig. 3** Microstructure of as-LMD GH 5188 specimens. **a** OM image, **b** schematic of heat flux, **c** SEM image, and **d** detailed cellular structure of **c**

Meanwhile, the growth direction of the columnar structure was oriented along the moving direction of the heat source. The difference in columnar growth direction in the adjacent deposited layers was due to the difference in the scanning strategy in the adjacent deposited layers. As shown in Fig. 3b, $D_x$ was related to the laser moving direction, $D_z$ was the heat flux direction along the substrate or previous layers, and $D_g$ was the resultant heat flux which was the columnar growth direction. Therefore, it was obvious that the columnar growth direction was mainly influenced by the heat flux of vertical and horizontal directions ($D_x$ and $D_z$). This result was in accordance with the previous experiment result for Inconel 718 fabricated by LMD [35].

SEM image in Fig. 3c showed that microstructure for the as-LMD GH 5188 specimens was composed of columnar and cellular structures. Cellular structures were attributed to a large temperature gradient and rapid solidification rate during LMD. As well-known, a molten pool was formed and then a large temperature gradient was created when the laser beam was applied to powders during the LMD process. With the laser beam moving, rapid solidification occurred immediately within the molten pool and then led to a large rapid solidification rate ($10^5 \sim 10^7$ K/s). Based on the grain growth mode, the higher ratio of the temperature gradient to rapid solidification rate was favorable to formation of cellular structures. Further details of columnar and cellular structures were shown in Fig. 3d, which revealed that the columnar structures were composed of sub-grains with a higher ratio of length to width whereas cellular structures consisted of equiaxed sub-grains. Additionally, it was obvious that the boundaries and sub-grains boundaries were decorated with chain-like precipitated phases. Chao et. al [36] pointed out that the chain-like precipitated phases were not a stable phase at elevated temperatures and they were easy to transform to granular morphology.

In order to identify the phase composition of as-LMD GH 5188 specimens, high-angle annular dark field SEM (HAADF) and selected area electron diffraction (SAED) TEM images were collected. Figure 4 presented the typical HAADF images and corresponding SAED TEM images of all phases in as-LMD GH 5188 specimens. The white phases should be confirmed as eutectic carbides which one for the $M_{23}C_6$ and $M_6C$ and the other for $M_{23}C_6$ and $La_2O_2C_2$. In the meantime, the matrix was identified to be γ phase. Therefore, the microstructure of as-LMD specimens was composed of three types of carbides and γ phase (Fig. 5).

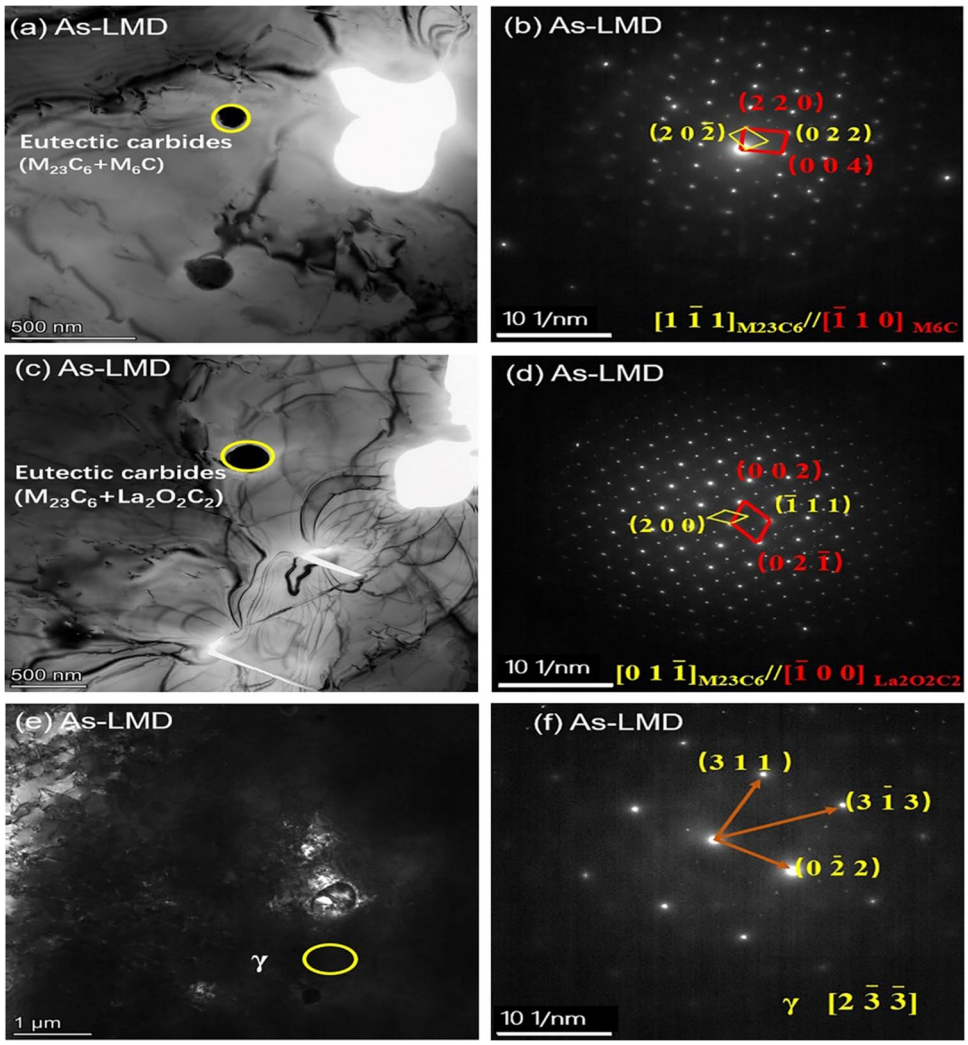


**Fig. 4** TEM images showing different eutectic carbides (**a**, **c**) and γphase (**e**) and corresponding SAED analysis (**b**, **d**, **f**)

Several studies dealt with the presence of the $La_2O_2C_2$ phase within GH 5188 superalloy. For example, Zeng et al. [37,38] pointed out that La and O elements showed strong affinity with each other, and thus, they preferentially formed $La_2O_3$ phases within the grains of GH 5188 superalloy. Meanwhile, during the solidification, C element easily combined with Ni, Cr, Co, and W elements to form $M_6C$-type carbides, but a little amount of C element still existed alone in the alloy. Additionally, the reaction to form $La_2O_2C_2$ was ever reported in reference [39,40]:

$$La_2O_3(s) + 3C(s) = La_2O_2C_2(S) + CO(g) \quad (1)$$

According to the above equation, the enthalpy of formation $La_2O_2C_2$ based on the appropriate thermodynamic date was calculated as $-320.0 \pm 2.0$ kcal/gfw [39]. Therefore, the presence of $La_2O_2C_2$ phase was reasonable for the as-LMD GH 5188 superalloy. Meanwhile, CO rapidly escaped due to the relatively short duration of the LMD process, and thus, the microstructure of as-LMD specimens had no cracks.

To study the effect of solution heat treatment on the microstructure of as-LMDed GH 5188 superalloy, OM micrographs of as-LMD GH 5188 specimens heat treated at different temperatures were examined, as shown in Fig. 6. From Fig. 5a the grain size was 51.1 μm and the grain shape was mainly columnar structure. Compared to as-LMD specimens (Fig. 3a), heat treatment at 1140 ℃ did not significantly change the grain size and shape. With the heat treatment temperature increasing to 1180 ℃ (Fig. 5b), the grain size showed grain growth with an average size of 84.1 μm, and columnar structure was gradually destroyed and altered to equiaxed grains. As Tucho et al. reported [41], when the heat treatment temperature was higher than 1100 ℃, the presence of recrystallization would occur within the SLMed superalloy. Therefore, for as-LMD GH 5188 specimens with heat treatment temperatures ranging from 1140 to 1180 ℃, the residual stress would relieve, and dislocation density would reduce during the as-deposition process and then transform the driving force of recrystallization, which

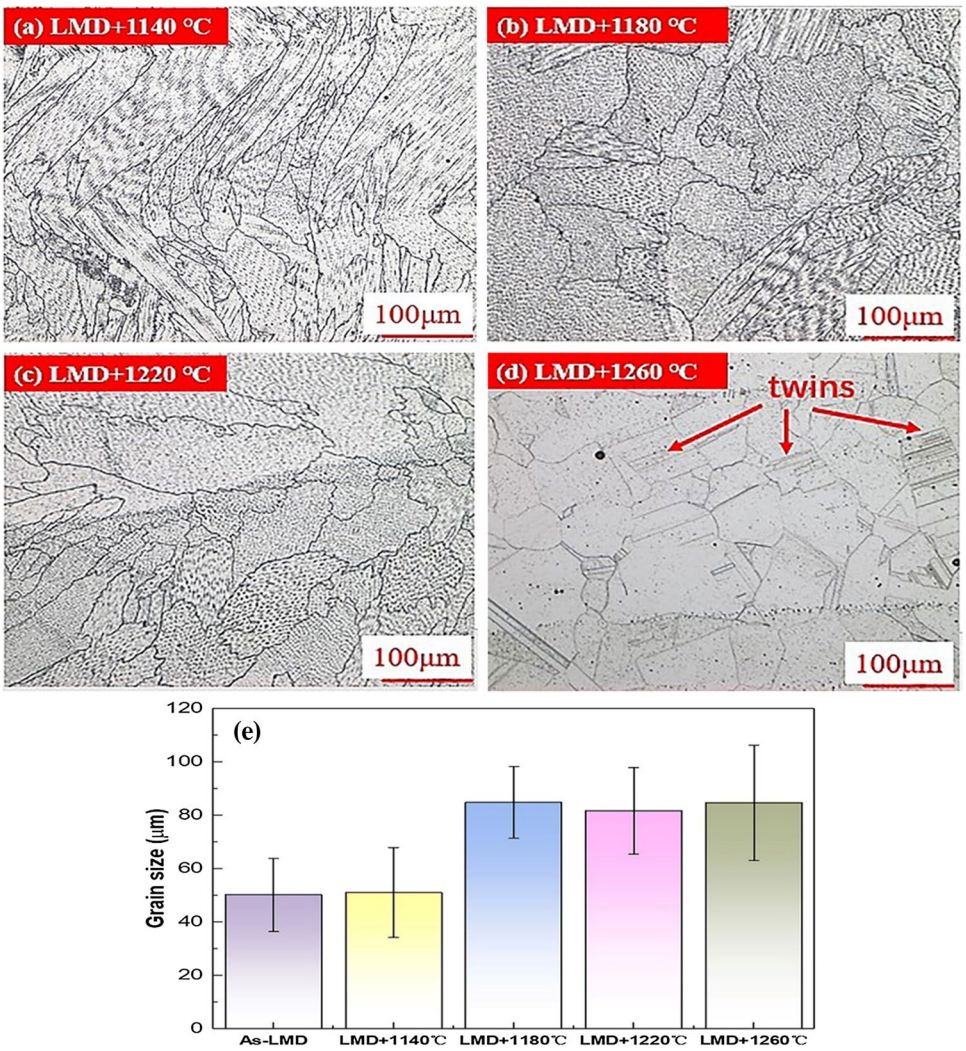


**Fig. 5** OM micrographs of as-LMD GH 5188 specimens heat treated at 1140 ℃ (**a**), 1180℃ (**b**), 1220℃ (**c**), 1260℃ (**d**), and grain size at different heat treatment temperatures (**e**)

contributed to grain coarsening [[42]]. Additionally, it was noticeable from Fig. 5c and d that the morphology of the grain boundary altered from the serrated grain boundary to the straight boundary as the heat treatment temperature increased from 1220 to 1260 ℃. Furthermore, the heat treatment temperature of 1260 ℃ resulted in the formation of annealing twins. This behavior was in accordance with the twins within the former study as-LMD IN 625 after annealing at 1025 ℃ [43]. As could be seen from Fig. 5e, the grain size grew bigger with the heat treatment temperature increasing from 1180 to 1260 ℃, but the grain sizes under these three temperatures were almost the same. The reason for grain sizes with no change under these three temperatures was that the higher heat treatment temperature would provide the stronger driving force to mainly dissolve carbides and facilitate twins formation [41].

Figure 6 presented the microstructure of as-LMD GH 5188 specimens treated at different solution temperatures. There was a noticeable phenomenon that carbide agglomeration would happen as the solution temperature treated at 1140 ℃, but carbides were dissolved when the temperature was further increased to above 1180 ℃. Additionally, carbides were mainly distributed in the inter-dendritic and intra-dendritic regions. Meanwhile, heat treatment temperature did not change the granular carbide morphology.

The volume fraction and the average size of carbides with respect to heat treatment temperatures were shown in Fig. 6e and f. It could be seen from Fig. 6e and f that the average size and the volume fraction of carbides were almost no change below the heat treatment temperature of 1180 ℃. However, the distinct difference was the more dispersed distribution of the carbides for the LMD + 1180 ℃ specimens. This was attributed to the higher heat treatment temperature, which would provide the stronger driving force to eliminate the segregation and destroy the dendrite structure. Increasing the heat treatment temperature to 1220℃, carbides were dissolved, and thus, its size and volume fraction decreased dramatically to 0.47 μm and 1.46%, respectively. Further

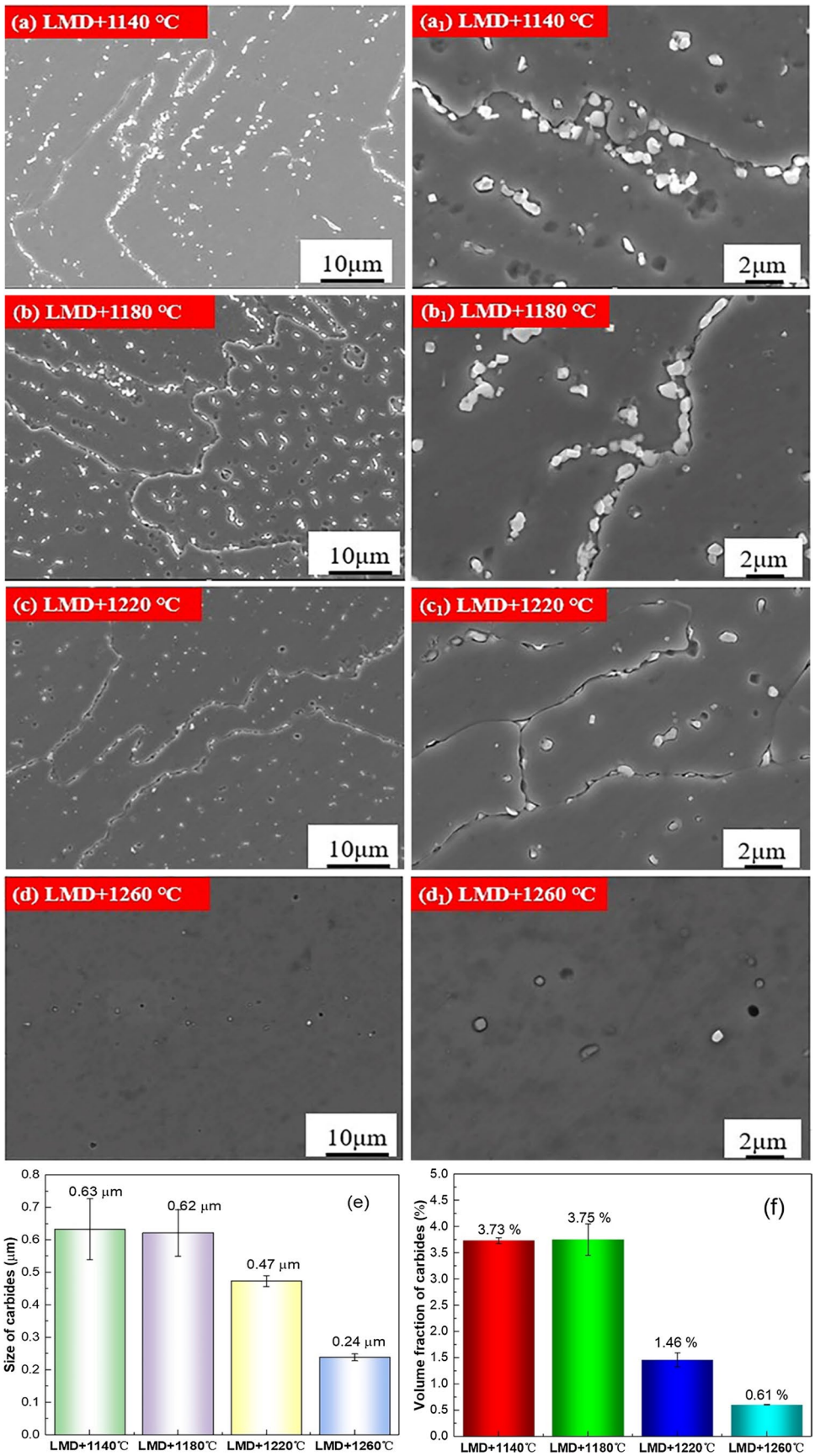


**Fig. 6** SEM micrographs of as-LMD GH 5188 specimens with heat treated at 1140℃ (**a**) ($a_1$), 1180℃ (**b**) ($b_1$), 1220℃ (**c**) ($c_1$), 1260℃ (**d**) ($d_1$), and volume fraction (**e**), and average size (**f**) of carbides with respect to different heat treatment temperatures

increase in heat treatment temperature to 1260 ℃ resulted in a further decreasing of the size (0.24 μm) and volume fraction (0.61%).

Figure 7 presented carbide morphology of as-LMD GH 5188 with heat treatment at different temperatures according to HAADF TEM images. It was found that carbides exhibited square and spherical morphology below the heat treatment temperature of 1180 ℃, while the morphology of carbides altered from square to spherical above 1180 ℃. This was attributed to the fact that the shape corner of white particles characterized by higher specific surface and higher internal energy would absorb more laser energy, resulting in its priority dissolution. Additionally, carbides mainly distributed in the inter-dendritic and intra-dendritic regions for all the heat treatment conditions.

HAADF micrograph and corresponding EDS mapping results of HT specimens with solution temperature at 1180 ℃ were shown in Fig. 8. A large amount of carbides was enriched with W, Cr, and C elements. Generally, $M_{23}C_6$ carbides were enriched with variable amount of Cr and C elements, and $M_6C$ carbides were enriched with Cr and C elements in the GH 5188 alloy [30]. Additionally, it was noticeable from Fig. 8 that some phases were enriched with O elements and their diameter were about 30 nm. The previous study ever pointed out that phases enriched with O elements were observable in the powder bed fused Inconel 718 before and after heat treatment [44].

The typical HAADF and SAED images of HT specimens with heat treatment at 1180℃ were shown in Fig. 9. As shown in Fig. 9A, B, C, and D, the precipitations were identified as $M_6C$-type and $M_{23}C_6$-type carbides and spherical carbides as $La_2O_2C_2$. Therefore, heat-treated specimens were composed of γ phase and three types of carbides, and heat treatment temperature does not significantly change the phases composition of as-LMD samples.

### 3.2 Tensile properties at room temperature

The fluorescent penetration result of as-LMD specimens was shown in Fig. 10. It was noticeable that the surface of as-LMD specimens was free of micro-cracks.

Finally, compared with the HT specimens' properties with different solution temperatures, the effect of different solution temperatures on stress–strain curves and tensile properties at room temperature was shown in Fig. 11. Evidently, UTS and EL of all HT specimens were higher than that of as-LMD specimens, indicating heat treatment improved both strength and elongation. This difference is believed to be caused by the fact that the chain-like precipitated phase has a negative effect on the mechanical properties [45]. From the results of HT specimens at different temperatures, the UTS is firstly enhanced and then decreased. Obviously, among all HT specimens, LMD + 1180 ℃ samples exhibited the highest UTS (1051.9 MPa). And the EL increased from 42.6 to 50.7% with the heat treatment temperature ranging from 1140 to 1180 ℃. Additionally, it was found from Fig. 7e to f that almost no change occurred with regard to the content and the size of carbides for the LMD + 1140 ℃

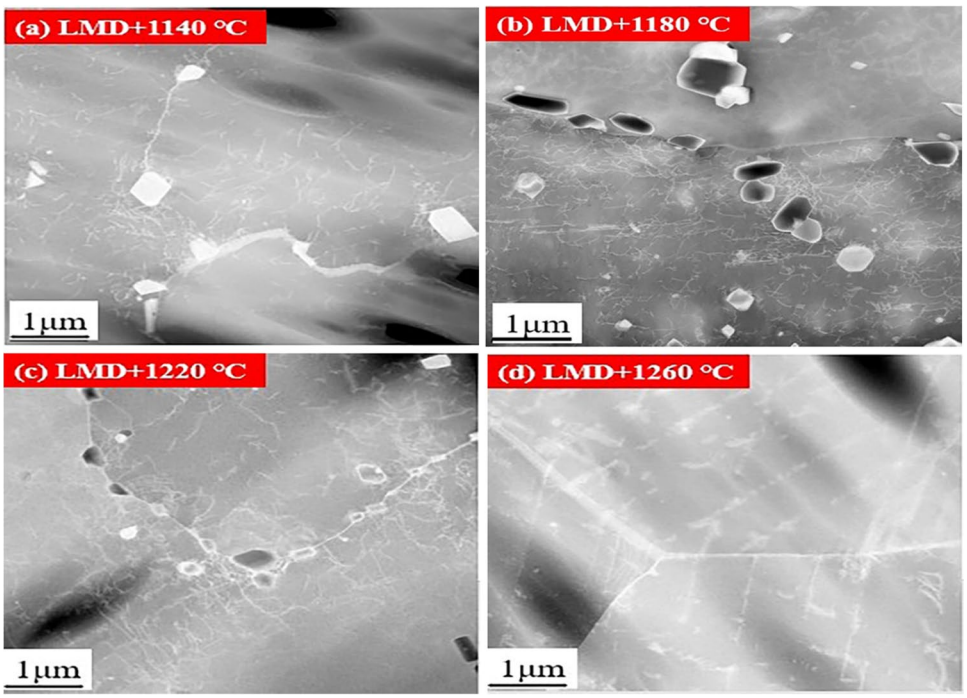


**Fig. 7** TEM images showing carbides morphology of as-LMD GH 5188 with heat treatment at different temperatures: (**a**) 1140 ℃, (**b**) 1180 ℃, (**c**) 1220 ℃, (**d**) 1260 ℃

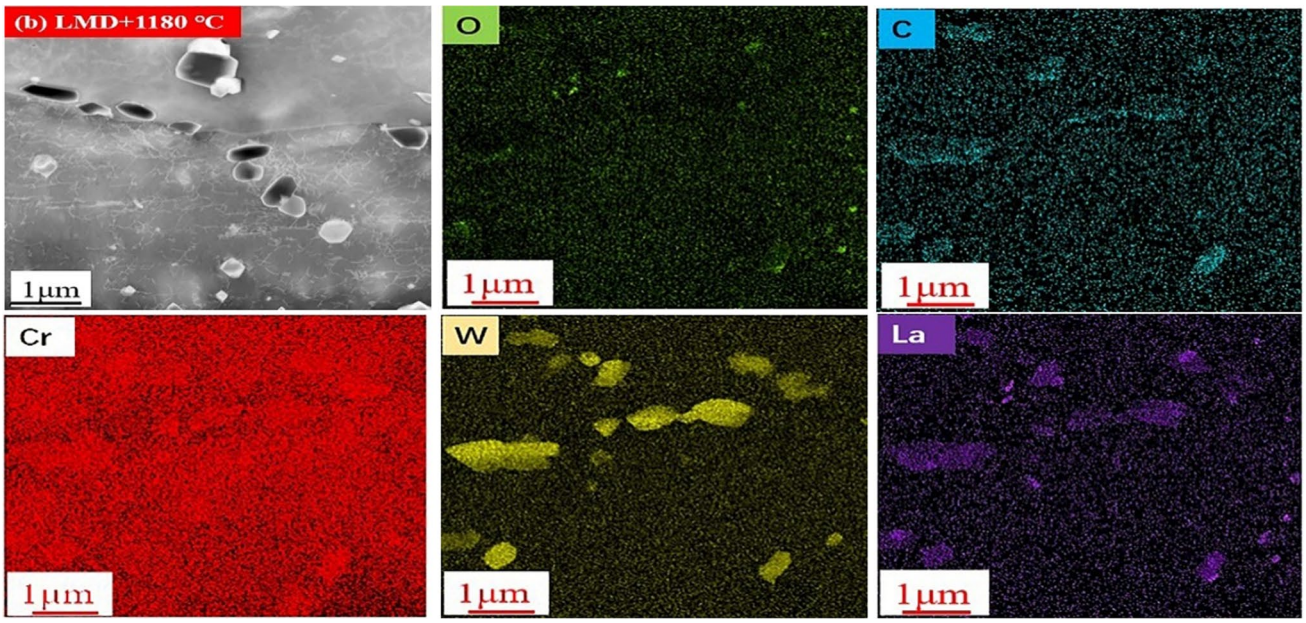


**Fig. 8** HAADF micrograph and corresponding energy-dispersive spectroscopy (EDS) mappings of LMD + 1180℃ specimens

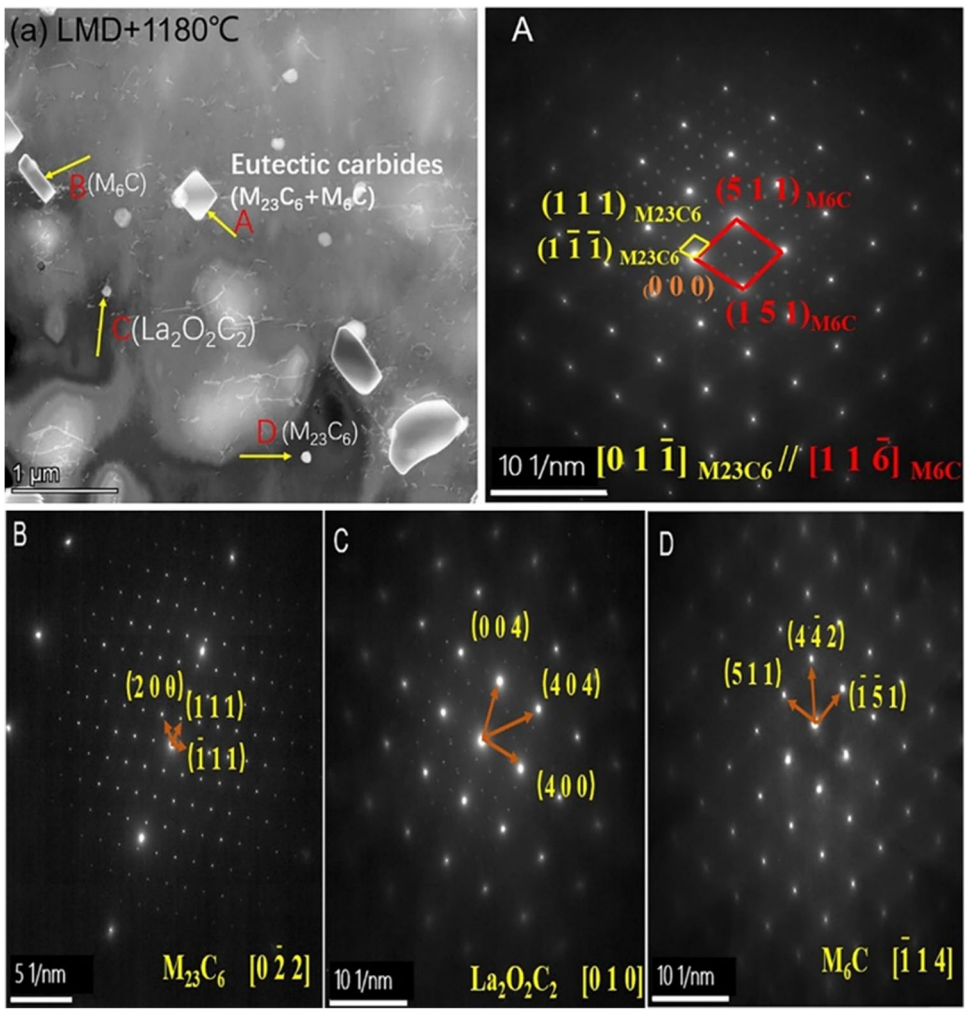


**Fig. 9** HAADF (**a**) and SAED images (**A**, **B**, **C**, **D**) of heat-treated specimens with heat treatment at 1180 ℃

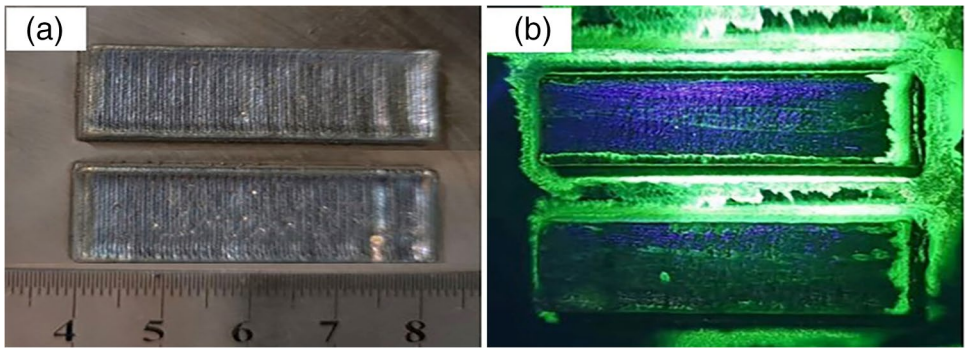


**Fig. 10** As-LMD specimens (**a**) and the corresponding fluorescent penetration result (**b**)

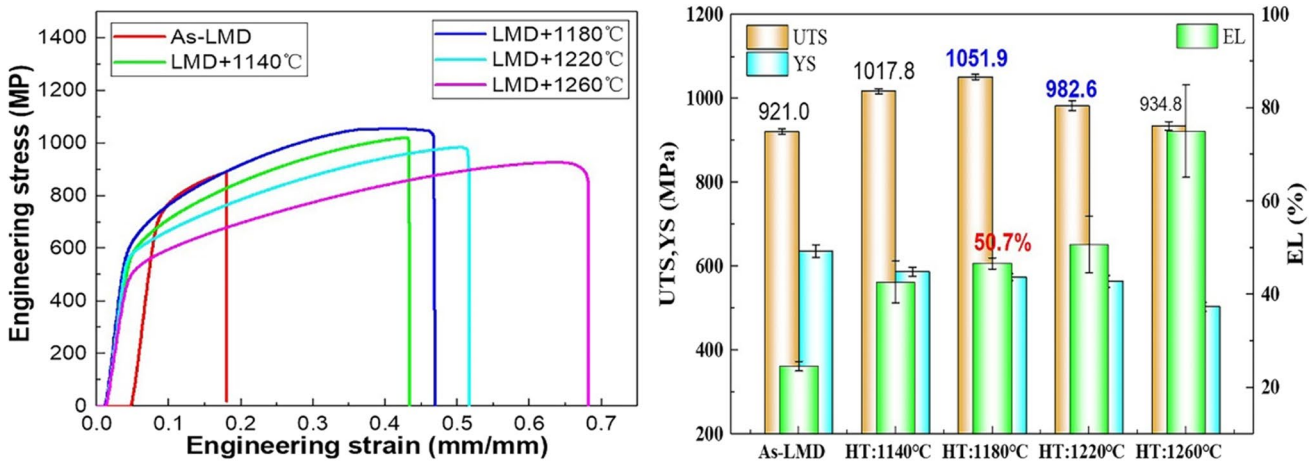


**Fig. 11** Effect of solution temperature on stress–strain curve and tensile property at room temperature of as-LMD and HT specimens

and LMD + 1180 ℃ HT specimens. Therefore, the increase in UTS below the heat treatment at 1180 ℃ was due to the dispersed distribution of carbides. In the case of heat treatment temperature at 1260 ℃, the EL was increased dramatically to 75%, but UTS was decreased obviously to 934.8 MPa and YS decreased to 503.6 MPa. The lowest UTS and YS values were attributed to the complete dissolution of carbides.

Additionally, YS values of all HT specimens were smaller than those of as-LMD specimens, and the YS decreased monotonously with the heat treatment temperature ranging from 1140 to 1260 ℃. The decrease of YS could be attributed to the fact that, the solution temperature was high enough to dissolve fully or partially the strengthening phases formed during the LMD process, resulting in the further weakening of YS for all HT specimens.

Meanwhile, Fig. 11 presented the relationship between EL and heat treatment temperatures of HT specimens. Based on the fact that carbides are brittle phases, their large size and high content will reduce the ductility of the material. Dispersed distribution and partial dissolution of carbides below the heat treatment at 1220 ℃ produced a slight improvement in ductility. The complete dissolution of the carbides in the LMD + 1260 ℃ specimens induced a significant improvement in ductility.

### 3.3 Fracture morphology of tensile tested specimens

Fracture surfaces of tensile tested specimens treated at different temperatures were examined by SEM. As could be seen in Fig. 12, the fracture surfaces of all HT specimens consisted of a number of dimples with different sizes, suggesting a ductile fracture feature. With the heat treatment temperature ranging from 1140 to 1260 ℃, the dimples became deeper, indicating better toughness. The LMD + 1140℃ specimens exhibited the lowest EL value (42.6%), while LMD + 1260℃ specimens showed excellent EL (75.0%).

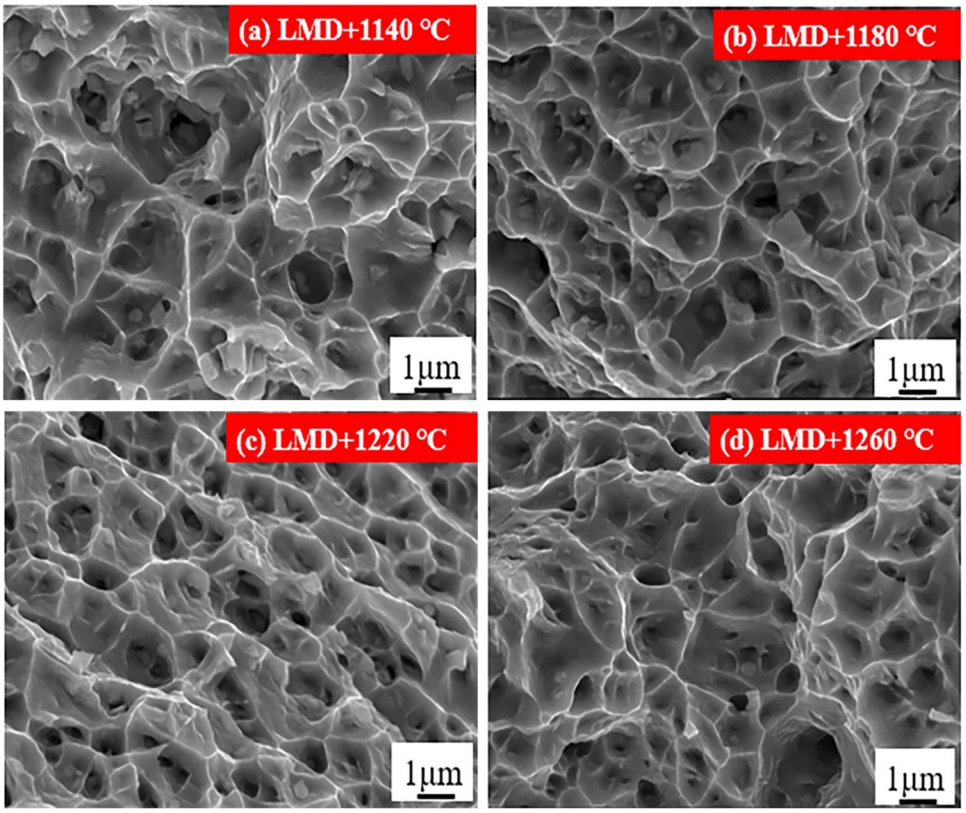


**Fig. 12** Fracture surfaces of tensile tested specimens with heat treatment temperature of 1140℃ (**a**), 1180℃ (**b**), 1220℃ (**c**), 1260℃ (**d**)

## 4 Conclusions

This study focused on the effect of heat treatment temperature on the microstructure and mechanical properties of GH 5188 fabricated by LMD. The main conclusions were summarized as follows:

(1) The dense GH 5188 superalloy specimens were fabricated by LMD successfully. The as-LMD alloys were mainly composed of γ, $M_{23}C_6$, $M_6C$, and $La_2O_2C_2$ regardless of the heat treatment temperature.
(2) Heat treatment temperature had an evident effect on the size and content of carbides. The size and volume fraction of carbides exhibited almost no change below 1180 ℃, while carbide size decreased dramatically from 0.62 to 0.24 μm, and the volume fraction of carbides decreased from 3.75 to 0.61% when the heat treatment temperature increased from 1180 to 1260℃
(3) Heat treatment improved both strength and elongation of as-LMD specimens. The EL was increased from 16.6 to 50.7%, and the UTS enhanced from 921.0 to 1051.9 MPa with the heat treatment temperature ranging from 1140 to 1180 ℃. In the case of heat treatment temperature at 1260 ℃, EL increased remarkably to 75%, but UTS decreased obviously to 934.8 MPa.
(4) All HT specimens exhibited a ductile fracture feature. With the heat treatment temperature ranging from 1140 to 1260 ℃, the dimples at the fractured surface become deeper, indicating better toughness.

**Funding** This work was supported by the Beijing Nova Program (Grant No. Z201100006820094) from the Beijing Municipal Science & Technology Commission and the National Natural Science Foundation of China (Grants No. 5177552, 52175369, and U2141205).

**Data availability** No data was used for the research described in the article.

## Declarations

**Conflict of interest** The authors declare no competing interests.

## References

1. Qu C, Zhou H, Zou X (2018) Experimental study on random vibration fatigue S-N curve of GH 188 alloy under high temperature environment. Adv Eng Res https://doi.org/10.2991/mecae-18.2018.42

2. Chen LJ, Liaw PK, He YH, Benson ML, Blust JW, Browning PF, Seeley RR, Klarstrom DL (2001) Tensile hold low-cycle fatigue behavior of cobalt-based Haynes ® 188 superalloy. Scr Mater 44:859–865. https://doi.org/10.1016/S1359-6462(00)00702-8
3. Rao K, Castelli MG, Ellis JR (1995) On the low cycle fatigue deformation of haynes 188 superalloy in the dynamic strain aging regime. Scr Metall Mater 33:1005–1012. https://doi.org/10.1016/0956-716X(95)00320-U
4. E.C.o.C.A.M. Handbook, China aeronautical materials handbook, Beijing: Standards Press of China, (2002),
5. Wang YQ, Suneson M (2013) Oxidation behavior of Hf-modified aluminide coatings on Haynes 188 at 1050 ° C. Surf Coat Technol 215:7–15. https://doi.org/10.1016/j.surfcoat.2012.07.091
6. Lee WS, Kao HC (2014) High temperature deformation behaviour of Haynes 188 alloy subjected to high strain rate loading. Mater Sci Eng A 594:292–301. https://doi.org/10.1016/j.msea.2013.11.076
7. Dong YP, Wang CY, Song XJ, Chen YH, Zhang MC, Wang SY (2013) Study on plastic deformation behavior of GH 5188 superalloy. Forg Stamping Technol 38:116–121. https://doi.org/10.3969/j.issn.1000-3940.2013.06.025
8. Liu DH, Chen JD, Chai HR, Jiang YH, Li Z, Qiu WQ, Guo ZH (2021) Study of meta-dynamic recrystallization behavior of GH 5188 superalloy. J Mater Res Technol 15:1179–1189. https://doi.org/10.1016/j.jmrt.2021.08.134
9. Bonacuse PJ, Kalluri S (1995) Elevated temperature axial and torsional fatigue behavior of Haynes 188. J Eng Mater Technol 117:191–199. https://doi.org/10.1115/1.2804529
10. Liu W, Xiong HP, Li N, Guo SQ, Qin RY (2018) Microstructure characteristics and mechanical properties of Nb-17Si-23Ti ternary alloys fabricated by in situ reaction laser melting deposition. Acta Metall Sin (Engl Lett) 31:28–36. https://doi.org/10.1007/s40195-017-0619-y
11. Zhang GD, Xiong HP, Yu H, Qin RY, Liu W, Yuan H (2020) Microstructure evolution and mechanical properties of wire-feed electron beam additive manufactured Ti-5Al-2Sn-2Zr-4Mo-4Cr alloy with different subtransus heat treatments. Mater Des 195:109063. https://doi.org/10.1016/j.matdes.-2020.109063
12. Zhang GD, Li N, Gao JS, Xiong HP, Yu H, Yuan H (2022) Wire-fed electron beam directed energy deposition of Ti–6Al–2Zr–1Mo–1V alloy and the effect of annealing on the microstructure, texture, and anisotropy of tensile properties. Addit Manuf 49:102511. https://doi.org/10.1016/j.addma.2021.102511
13. Yang T, Tomus D, Rometsch P, Wu X (2017) Influences of processing parameters on surface roughness of Hastelloy X produced by selective laser melting. Addit Manuf 13:103–112. https://doi.org/10.1016/j.addma.2016.10.010
14. Liu W, Ren XY, Li N, Gao C, Xiong HP (2021) Rapid directionally solidified microstructure characteristic and fracture behaviour of laser melting deposited Nb–Si–Ti alloy. Prog Nat Sci Mater Int 31:113–120. https://doi.org/10.1016/-j.pnsc.2020.12.003
15. Miyake M, Matsuda T, Sano T, Hirose A, Shiomi Y, Sasaki M (2020) Microstructure and mechanical properties of additively manufactured CoCrW alloy using laser metal deposition. Weld World 64:1397–1407. https://doi.org/10.1007/s40194-020-00926-y
16. Li N, Liu W, Wang Y, Zhao ZJ, Yan TQ, Zhang GH, Xiong HP (2021) Laser additive manufacturing on metal matrix composites: a review. Chin J Mech Eng 34:1–16. https://doi.org/10.1186/s10033-021-00554-7
17. Li N, Huang S, Zhang GD, Qin RY, Liu W, Xiong HP, Shi GQ, Blackburn J (2019) Progress in additive manufacturing on new materials: a review. J Mater Sci Technol 35:242–269. https://doi.org/10.1016/j.jmst.2018.09.002
18. Wang XY, Liu ZD, Li JY, Chen L, Li BK (2022) Effect of heat treatment on microstructure, corrosion resistance, and interfacial characteristics of Inconel 625 laser cladding layer. Optik 270:169930. https://doi.org/10.1016/j.ijleo.2022.169930
19. Guevenoux C, Hallais S, Charles A, Charkaluk E, Constantinescu A (2020) Influence of interlayer dwell time on the microstructure of Inconel 718 laser cladded components. Opt Laser Technol 128:106218. https://doi.org/10.1016/j.optlastec.2020.106218
20. Jinoop AN, Paul CP, Bindra KS (2019) Laser assisted direct energy deposition of Hastelloy-X. Opt Laser Technol 109:14–19. https://doi.org/10.1016/j.optlastec.2018.07.037
21. Bi G, Sun CN, Chen HC, Ng FL, Ma CK (2014) Microstructure and tensile properties of superalloy IN 100 fabricated by micro-laser aided additive manufacturing. Mater Des 60:401–408. https://doi.org/10.1016/j.matdes.2014.04.020
22. Zhang XQ, Chai Z, Chen HB, Xu JJ, Xu LM, Lu H, Chen XQ (2021) A novel method to prevent cracking in directed energy deposition of Inconel 738 by in-situ doping Inconel 718. Mater Des 197:109214. https://doi.org/10.1016/j.matdes.2020.109214
23. Gong XY, You W, Li X, Wang L (2020) Modeling the influence of injection parameters on powder efficiency in laser cladding. Weld World 64:1437–1448. https://doi.org/10.1007/s40194-020-00955-7
24. Joseph C, Persson C, Colliander MH (2017) Influence of heat treatment on the microstructure and tensile properties of Ni-base superalloy Haynes 282. Mater Sci Eng A 679:520–530. https://doi.org/10.1016/j.msea.2016.10.048
25. Wang Y, Li N, Jia CL, Liu W, Wu Y, Gao C, Xiong HP (2022) Effects of solution treatment on the microstructural evolution and tensile properties of GH 3230 superalloy manufactured by laser melting deposition. Mater Charact 194:112339. https://doi.org/10.1016/j.matchar.2022.112339
26. Qiao G, Zhang B, Bai Q, Dilnoza Y (2021) Effect of heat treatment on microstructure and residual stress of GH 3536 superalloy fabricated by selective laser melting. J Mater Eng Perform 30:8892–8900. https://doi.org/10.1007/s11665-021-06094-4
27. Yin YY, Zhang JH, Huo JX, Zhao K, Zhu XM, Meng XY, Han QQ, Ma YC, Fu ZS, Yin JC (2020) Effect of microstructure on the passive behavior of selective laser melting fabricated Hastelloy X in $NaNO_3$ solution. Mater Charact 165:110370. https://doi.org/10.1016/j.matchar.2020.110370
28. Liu W, Huang S, Ye C, Jia L, Kang Y, Sha J, Chen B, Wu Y, Xiong H (2023) Progress in Nb-Si ultra-high temperature structural materials: a review. J Mater Sci Technol. https://doi.org/10.1016/j.jmst.2022.11.022
29 Wei W, Xiao JC, Wang CF, Cheng Q, Guo FJ, He Q, Wang MS, Jiang SZ, Huang CX (2022) Hierarchical microstructure and enhanced mechanical properties of SLM-fabricated GH 5188 Co-superalloy. Mater Sci Eng A 831:142276. https://doi.org/10.1016/j.msea.2021.142276
30. Zheng XH, Chen X, Zhai Y, Cheng Q, Guo FJ, He Q, Su WL, Zhang C, Ran H (2022) The anisotropy of mechanical properties response on crystallographic features of GH 5188 superalloy fabricated by laser powder bed fusion. Soc Sci Electron Pub. https://doi.org/10.2139/ssrn.4035130.
31. Xu L, Chu J, Wang J, Zhou Y, Wang D (2022) Effects of process parameters on density of GH 5188 high-temperature alloy after selective laser melting. J Phys: Conf Ser. 012077, https://doi.org/10.1088/1742-6596/2355/1/012077.
32. Liu C, Guo KK, Zhang YL, Shang S, Liu CS (2021) Influence of energy density on the microstructure and mechanical properties of GH 5188 superalloy formed by laser melting deposition. Fourth International Symposium on High Power Laser Science and En (HPLSE 2021), 262–268, https://doi.org/10.1117/12.2599108.
33. Yan ZW, Trofimov V, Song CH, Han CJ, Yang YQ, Yang C, Xiao Y, Deng ZT, Chen J (2023) Microstructure and mechanical properties of GH 5188 superalloy additively manufactured via

ultrasonic-assisted laser powder bed fusion. J Alloys Compd 939:168771. https://doi.org/10.1016/j.jallcom.2023.168771
34. Eissel A, Engelking L, Treutler K, Schroepfer D, Wesling V, Kannengiesser T (2023) Investigations on influencing the microstructure of additively manufactured Co-Cr alloys to improve subsequent machining conditions. Weld World 67:1081–1089. https://doi.org/10.1007/s40194-022-01397-z
35. Parimi LL, Ravi GA, Clark D, Attallah MM (2014) Microstructural and texture development in direct laser fabricated IN718. Mater Charact 89:102–111. https://doi.org/10.1016/j.matchar.2013.12.012
36. Zhao C, Wang Z, Li DX, Kollo L, Luo ZQ, Zhang WW, Prashanth KG (2020) Cu-Ni-Sn alloy fabricated by melt spinning and selective laser melting: a comparative study on the microstructure and formation kinetics. J Mater Res Technol 9:13097–13105. https://doi.org/10.1016/j.jmrt.2020.09.047
37. Zeng BS, Wu SQ, Zhang SL (1986) Role and distribution of La in Co-base superalloy GH 188. J Chin Rare Earth Soc 04:48–55
38. Zeng BS, Wu SQ, Zhang SL (1986) Effect of C and La content on the structures and properties of cobalt-base superalloy GH 188. J Iron Steel Res 02:30–36
39. Butherus AD, Eick HA (1973) Preparation, characterization, and some thermodynamic properties of lanthanum oxide carbide, $La_2O_2C_2$. J Inorg Nucl Chem 35:1925–1930. https://doi.org/10.1016/0022-1902(73)80128-9
40. Seiver RL, Eick HA (1976) The crystal structure of dilanthanum dioxidedicarbide, $La_2O_2C_2$. J Less-Common Met 44:1–9. https://doi.org/10.1016/0022-5088(76)90113-2
41. Tucho WM, Cuvillier P, Sjolyst-Kverneland A, Hansen V (2017) Microstructure and hardness studies of Inconel 718 manufactured by selective laser melting before and after solution heat treatment. Mater Sci Eng A 689:220–232. https://doi.org/10.1016/j.msea.2017.02.062
42 Tomus D, Tian Y, Rometsch PA, Heilmaier M, Wu XH (2016) Influence of post heat treatments on anisotropy of mechanical behaviour and microstructure of Hastelloy-X parts produced by selective laser melting. Mater Sci Eng A 667:42–53
43. Sukumaran A, Gupta RK, Kumar VA (2017) Effect of heat treatment parameters on the microstructure and properties of Inconel 625 superalloy. J Mater Eng Perform 26:3048–3057. https://doi.org/10.1007/s11665-017-2774-8
44. Zhou L, Mehta A, McWilliams B, Cho K, Sohn Y (2019) Microstructure, precipitates and mechanical properties of powder bed fused inconel 718 before and after heat treatment. J Mater Sci Technol 35:1153–1164. https://doi.org/10.1016/j.jmst.2018.12.006